https://doi.org/10.1016/j.ijfatigue.2023.107961


# Cyclic elastoplasticity and XFEM based fatigue life assessment of out-of-plane gusset welded joints

Yixun Wang[1,*], Riccardo Fincato[2], Yuki Kotani[3], Seiichiro Tsutsumi[2,*], Tak-Ming Chan[1]

[1] *Department of Civil and Environmental Engineering, The Hong Kong Polytechnic University, Hong Kong, China*
[2] *Department of Civil Engineering, Osaka University, Osaka, Japan*
[3] *KAWADA Industries, Inc., Kagawa, Japan*

**Abstract:** Conventional design methods for high-cycle fatigue failure of engineering components often assume a linear-elastic material behaviour. The different driving forces of crack initiation and propagation fail to be considered, resulting in less accurate predictions of fatigue life. To address this issue, the present study proposes a novel method to predict the fatigue life of out-of-plane gusset welded joints based on cyclic elastoplasticity and extended finite element method (XFEM). Incorporating the welding residual stress simulated by thermal-mechanical analysis, the cyclic stress-strain response of out-of-plane gusset welded joints was assessed by Fatigue SS (FSS) constitutive model. The crack initiation life was therefore predicted by the local strain approach considering the mean stress correction. Based on the converged cyclic stress-strain response, the crack propagation behaviour and life were predicted by XFEM in combination with Virtual Crack Closure Technique (VCCT). The influence of mean stress, mixed-mode crack and residual stress on crack initiation and propagation life was also investigated. The results show that the proposed method can predict the fatigue life of out-of-plane gusset welded joints under the pure tension loading with high accuracy against experimental results.

**Key words**: fatigue life, gusset welded joints, cyclic elastoplasticity, extended finite element method (XFEM), mean stress

* Corresponding author, E-mail: yixun.wang@polyu.edu.hk (Y. Wang); tsutsumi@civil.eng.osaka-u.ac.jp (S. Tsutsumi)

## 1 Introduction

Steel bridges are extensively used for bridge engineering due to their favourable characteristics such as high strength, long-span capability, fast construction and low cost [1]. Because of the nature of the thin-walled structure, the steel bridge deck, flange and web are often stiffened by the out-of-plane gusset to enhance bearing capacity and avoid local buckling [2-3]. Under the cyclic vehicle loading, the out-of-plane gusset welded joints are susceptible to fatigue cracking due to the combined effects of residual stress, stress concentration and weld defects, which have been widely reported in steel bridges [4-5]. Fig. 1 shows some typical fatigue cracks of out-of-plane gusset welded joints observed in steel bridges. The cracks often initiate from the weld toe with high stress concentration, and then propagate towards the base metal, resulting in the sudden failure of steel components and endangering the service safety of steel bridges. Therefore, it is essential to assess the fatigue life of out-of-plane gusset welded joints with high accuracy for the purpose of structural design and maintenance.

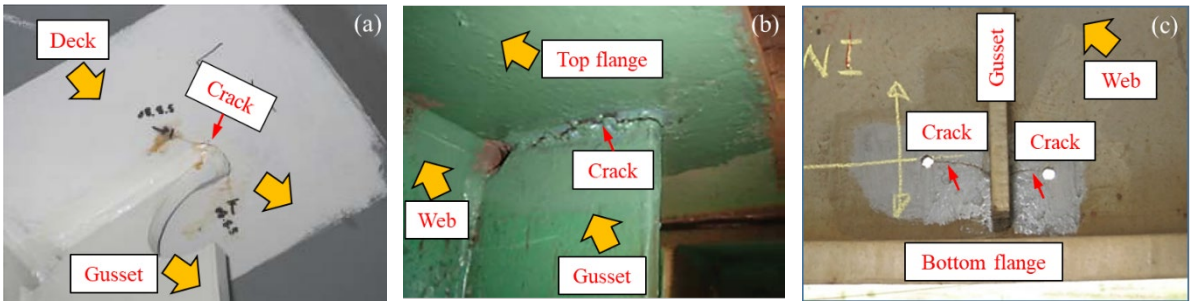


Fig. 1 Typical fatigue cracks of out-of-plane gusset welded joints detected on the (a) bridge deck [6] (b) girder flange [7] (c) girder web [8]

The fatigue failure of out-of-plane gusset welded joints involves the stages of crack initiation and crack propagation [9-10], which are governed by different driving forces. The crack initiation is a material surface phenomenon, and the crack nucleation or micro crack growth are mainly determined by the geometric discontinuity and surface roughness [11]. The crack propagation, usually referring to the macro crack growth, depends on the crack growth resistance of the material as a bulk property [12]. The nominal stress method

is widely used for convenient application in real engineering, whilst the predicted fatigue life often shows great divergence in many references [13-15]. The hot spot stress method, taking the structural features into consideration, is suitable to assess the welded joints without clear definition of the nominal stress. Yamamoto [16] pointed out that the fatigue life of out-of-plane gusset welded joints could be overestimated if assessed by the hot spot stress method due to thickness effects. Incorporating the influence of stress concentration due to bead geometry, Park [17] assessed the fatigue life of out-of-plane gusset welded joints by the effective notch stress method, and proposed to distinguish the crack initiation position based on the maximum principal stress. To improve the accuracy of effective notch stress method, Wang [18] proposed a modified notch stress method considering the real bead geometry, which was proved to be applicable to as-welded and additional-welded conditions. The above-mentioned methods assessed the crack initiation and propagation life as a whole without considering different cracking mechanisms. The precision of fatigue life assessment is far from being satisfactory. There are still few reports [19-21] concerning separate assessment of crack initiation and propagation life of out-of-plane gusset welded joints.

Analytical method is convenient to predict the crack propagation life of welded joints, whilst it is not flexible to assess the complex welded structures without the standard formulae for the stress intensity factor (SIF). The existing literature on crack propagation assessment of out-of-plane gusset welded joints often involves the finite element analysis (FEA) based on linear elastic fracture mechanics (LEFM) [22]. Choi [23] suggested a strain energy density factor approach, considering the influence of initial crack shape, crack length and mean stress, and the predicted crack shapes agreed well with the experimental results. For multiaxial fatigue conditions such as biaxial loadings with phase difference, Gotoh [24] proposed to assess the crack growth of out-of-plane gusset welded joints by an equivalent distributed stress method. Wang [8] studied the mixed-mode crack propagation of out-of-plane gusset welded joints using the extended finite

element method (XFEM), and highlighted the influence of the welding residual stress on the accuracy of fatigue life assessment. Although influence of the welding residual stress is increasingly discussed in recent research [25-27], it should be noted that welding residual stress is relaxed during the cyclic loading and finally converged at a quite different distribution from the original one. Tchuindjang [28] pointed out that welding tensile residual stress became compressive at the weld toe of out-of-plane gusset after the first loading cycle and strongly affected the crack closure. Nevertheless, the influence of converged residual stress incorporating the mean stress and local stress concentration on crack propagation rate of out-of-plane gusset welded joints is not yet reported.

Due to the limitations as explained above, this paper proposed a novel method to predict the fatigue life of out-of-plane gusset welded joints. The fatigue experiments conducted on the out-of-plane gusset welded joints made of Grade 345 steel were referred for verification. Firstly, the welding simulation based on the real welding condition was carried out. The welding residual stress distribution obtained by the thermal-mechanical FEA was defined as the initial stress state for structural analysis. Secondly, the material constants of the Fatigue SS (FSS) constitutive models for the weld metal (WM) and base metal (BM) were embedded into the FE model. The cyclic loading was performed to obtain the converged stress-strain response at the weld toe, by which the position with the minimum crack initiation life could be identified. Thirdly, initial crack was embedded into the FE model for crack propagation analysis by XFEM in combination with the virtual crack closure technique (VCCT), taking the converged stress-strain response as the initial state. The crack propagation life was assessed by the Paris law [29] with the correction of mean stress and mixed-mode crack. Therefore, the fatigue failure life was predicted by the sum of crack initiation life and propagation life. This research is expected to improve the accuracy of the fatigue life assessment for the out-of-plane gusset welded joints and expand the horizon for fatigue design.

## 2 Methodology

### 2.1 Crack initiation analysis based on FSS constitutive model

The crack initiation life $N_c$ is often predicted by the local strain method which requires an accurate assessment of the cyclic stress-strain response at the position of the crack initiation. Tsutsumi [30] proposed a constitutive model (FSS model) for predicting stress-strain relationships under the fatigue loading to include the softening behaviour for low stress amplitudes within the macroscopic yield stress. The FSS model shows good accuracy for high-cycle fatigue problems of steel with different grades. The FSS model was established based on the subloading surface theory [31] as seen in Fig. 2. Unlike the normal yield surface in the classic plasticity theory, a subloading surface was defined to allow the occurrence of plastic deformation under the cyclic loading conditions below the macroscopic yield stress. The subloading surface was created by means of a similarity transformation from the normal yield surface. Specifically, the similarity centre $\boldsymbol{s}$ moves in the stress space following the development of inelastic strain, allowing a realistic description of the plastic accumulation in cyclic mobility problems. The yield condition of normal yield surface is defined by Eq. (1) as follows:

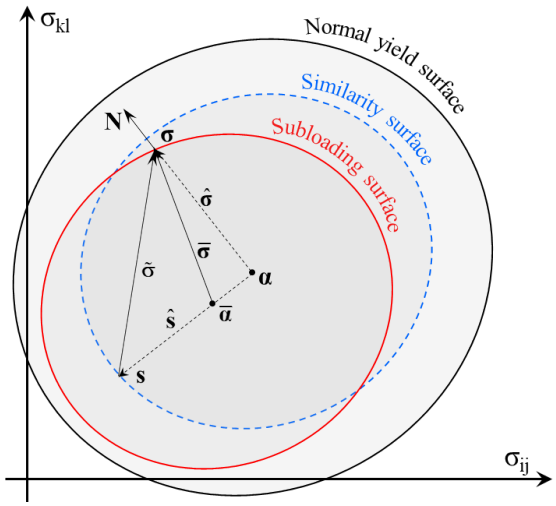


Fig. 2 Illustration of FSS constitutive model [30]

$$f(\hat{\boldsymbol{\sigma}}) = F(H),\ \hat{\boldsymbol{\sigma}} = \boldsymbol{\sigma} - \boldsymbol{\alpha} \tag{1}$$

$$F(H) = F_0\left[1 + h_1\left\{1 - \exp^{(h_2 H)}\right\}\right] \tag{2}$$

where $\boldsymbol{\sigma}$ denotes the Cauchy stress tensor, $\boldsymbol{\alpha}$ denotes the back stress, $\hat{\boldsymbol{\sigma}}$ denotes the stress tensor translated by the back stress. The isotropic hardening rule *F(H)* is defined by Eq. (2), where *H* denotes the cumulative plastic strain, $F_0$ denotes the initial size of the normal yield surface, $h_i$ ($i$ = 1,2) controls the evolution rate of isotropic hardening. The similarity ratio *R* of the normal yield surface to the subloading surface is defined by Eq. (3).

$$f(\overline{\boldsymbol{\sigma}}) = RF(H),\ \overline{\boldsymbol{\sigma}} = \boldsymbol{\sigma} - \overline{\boldsymbol{\alpha}},\ \overline{\boldsymbol{\alpha}} = \boldsymbol{s} - R\hat{\boldsymbol{s}},\ \tilde{\boldsymbol{\sigma}} = \boldsymbol{\sigma} - \boldsymbol{s},\ \hat{\boldsymbol{s}} = \boldsymbol{s} - \boldsymbol{\alpha} \tag{3}$$

where $\tilde{\boldsymbol{\sigma}}$ and $\overline{\boldsymbol{\sigma}}$ denote the conjugated stress tensor of the $\boldsymbol{s}$ surface and subloading surface, respectively, and $\hat{\boldsymbol{s}}$ denotes the similarity-centre tensor observed from the back stress. Moreover, to predict the cyclic stress-strain response of materials that have definite elastic behaviour (for example, metals), the concept of elastic boundary $R_e$ is introduced by Eq. (4) [32] so that there is no plastic deformation when $R < R^e$. The implementation of FSS constitutive model is elaborated in Eq. (5)-(9) [30]. The evolution of *R* is defined by Eq. (5).

$$\begin{cases} R = 0 & \text{null stress state} \\ 0 < R < R_e & \text{quasi-elastic stress state} \\ R_e < R < 1 & \text{sub-yield stress state} \\ R = 1 & \text{normal-yield stress state} \end{cases} \tag{4}$$

$$\dot{R} = U(R)\left|\boldsymbol{D_P}\right|,\ U(R) = u\cot\left(\frac{\pi\left\langle R - R_e\right\rangle}{2(1 - R_e)}\right) \tag{5}$$

where $\boldsymbol{D_p}$ denotes the plastic strain rate, $u$ denotes the material constant and 〈〉 denotes the Macauley's brackets. The cyclic hardening or softening of materials due to the cumulative plastic strain is described by the cyclic damage function *D* as Eq. (6):

$$D(H_d) = (1 - d_2)\left[1 + \left(d_1 / H_d\right)^{d_3}\right]^{-1} \tag{6}$$

where $d_i$ ($i$ = 1,2,3) denotes the material constants which control the damage rate, and $H_d$ denotes the cyclic

damage in the form of plastic work, by which the opening and expansion of hysteresis loop are made possible. The evolution of $H_d$ is defined by Eq. (7).

$$H_d = \int \sqrt{2/3}\left|\boldsymbol{D_P}\right|\bar{D}dt \tag{7}$$

$$\bar{D}(\bar{R}) = (1-k_2)\left[1+(k_1/\bar{R})^{k_3}\right]^{-1}, \quad \bar{R} = R - R_e \tag{8}$$

where $t$ denotes the genetic time, the scalar $\bar{D}$ is defined in Eq. (8) to control the damage amount that occurs within the subloading surface, and $k_i$ ($i$ = 1,2,3) denotes the material constants which should be calibrated based on the fatigue tests. The cyclic accumulated damage work $\bar{D}$ is monotonically increased with increasing of $R$ and asymptotic with respect to $\bar{D}_{max}$ =1 - $k_2$. The nonlinear kinematic hardening rule is defined by Eq. (9).

$$\dot{\boldsymbol{\alpha}} = a_1(a_2\boldsymbol{N} - \boldsymbol{\alpha})\left[1 + a_3\left(1 - \frac{\left\langle R - R_e \right\rangle}{1 - R_e}\right)\right]\left\|\boldsymbol{D_P}\right\| \tag{9}$$

where $\boldsymbol{N}$ denotes the outward normalised normal tensor to the subloading surface at the current stress state, and $a_i$ ($i$ = 1,2,3) denotes the material constants which should be calibrated based on the fatigue tests. The FSS constitutive model has the predominant advantage of describing appropriately the material behaviour under cyclic loading in both sub-yield and fully plastic stress states without necessity of using different material characterisations [33]. Morita [34] predicted the converged stress-strain response of the Grade 345 steel in both sub-yield and fully plastic stress states based on the FSS constitutive model. The comparison between the prediction and the experimental results in Fig. 3 shows that the high accuracy of prediction can be achieved for both large and limited plastic deformation. Therefore, the calibrated materials constants for BM and WM of Grade 345 steel based on the FSS constitutive model (Table 1) were used in the subsequent analysis to assess the cyclic stress-strain response at the weld toe for fatigue life prediction.

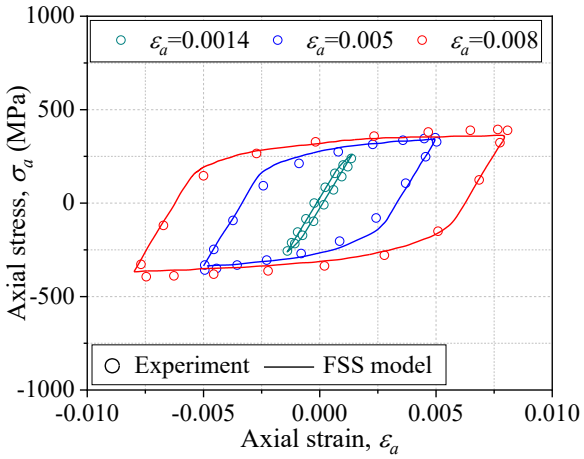


Fig. 3 Cyclic response predicted by FSS model [34]

Table 1 Calibrated FSS model parameters of the WM and BM of the Grade 345 steel

| Materials | Initial yield surface | Isotropic hardening | | Kinematic hardening | | | Damage function | | | $\bar{D}$ function | | |
|---|---|---|---|---|---|---|---|---|---|---|---|---|
| | $F_0$ | $h_1$ | $h_2$ | $a_1$ | $a_2$ | $a_3$ | $d_1$ | $d_2$ | $d_3$ | $k_1$ | $k_2$ | $k_3$ |
| WM | 520 | 0.0 | 0.0 | 5.0 | 500 | 1.0 | 0.0001 | 0.006 | 1.0 | 0.6 | 0.5 | 8.0 |
| BM | 336 | 0.1 | 4.0 | 1.0 | 740 | 1.0 | 0.0004 | 0.0096 | 2.0 | 0.6 | 0.5 | 6.77 |

## 2.2 Crack propagation analysis by XFEM in combination with VCCT

The crack propagation life $N_p$ of the welded joints in the high cycle fatigue regime can often be assessed by the LEFM due to the small-scale plastic condition. The XFEM [35] models discontinuities as an enriched feature to simulate the crack propagation along an arbitrary, solution-dependent path without mesh regeneration during the crack propagation. The enrichment functions consist of a near-tip asymptotic function to capture the singularity of the crack tip and a discontinuous function to describe the displacement through the crack surfaces. The detailed description of XFEM is found in [36]. The XFEM can be implemented based on the LEFM for high cycle fatigue problems. The strain energy release rate, which serves as the crack driving force in LEFM, can be calculated based on the VCCT. The VCCT assumes that the released strain energy when a crack grows by a certain length is equal to the energy required to close the crack by the same amount [37]. Therefore, the strain energy release rate can be calculated, and the corresponding SIF $K$ is obtained by the assumption of linear elasticity. Considering the mixed-mode fatigue

crack propagation in the real welded joints, the equivalent SIF $K_{eq}$ is expressed by Eq. (10) [38].

$$\Delta K_{eq} = \sqrt{\Delta K_I^2 + \Delta K_{II}^2 + \Delta K_{III}^2} \tag{10}$$

$$\frac{da}{dN} = C_0 \left( \frac{\Delta K_{eq}}{(1-R)^{1-\gamma}} \right)^m, R = \frac{K_I^{\min}}{K_I^{\max}} \tag{11}$$

where, $\Delta K_I$, $\Delta K_{II}$, and $\Delta K_{III}$ are SIF ranges corresponding to the crack mode I, II and III conditions, respectively. It is assumed that energy required to advance the crack tip straight ahead is equivalent to the energy available for propagating the crack at some other angle under the crack mode I condition. Finally, the crack propagation rate can be described by the Paris law [29] with the correction of stress ratio $R$ proposed by Walker [39], as seen in Eq. (11). Where, $da/dN$ indicates the crack propagation rate, $C_0 = 5.21\times10^{-13}$, $m$ = 3.0 as recommended by IIW [40], and $\gamma = 0.789$ as proposed by Xin [41]. It should be noted that the stress ratio $R$ was defined by the SIF of mode I ($K_I$) in this research, which is the dominated cracking mode as detailed in Section 5.2.

The performance of XFEM and VCCT to predict the fatigue crack propagation behaviour was verified by comparing to the analytical method. A compact tension (CT) specimen was modelled to conduct the simulation of crack propagation analysis. The dimensions of the CT specimen are shown in Fig. 4. A through-thickness crack was defined with initial length of 5.0 mm. Xin [42] recommended that the convergence of *a*-*N* relationship can be achieved with the local mesh size no larger than 1.0 mm. Therefore, the mesh size in the enrichment area (XFEM region) was decided to be 1.0 mm and the global mesh size was 2.0 mm. To improve the computational efficiency, the full-integration element C3D8 was used in the enrichment area whilst the reduced integration element C3D8R was used in other regions. The FE model of the CT specimen is shown in Fig. 5. Referring to the analysis of boundary conditions in [42], the vertical cyclic loading was applied on the reference point *RP*1 coupled to the top half cycle of the circular hole. The rotation around X-

axis and Y-axis was constrained. The reference point *RP*2 was coupled to the bottom half cycle of the circular hole with the displacement in Y-axis and rotation around X-axis and Y-axis constrained.

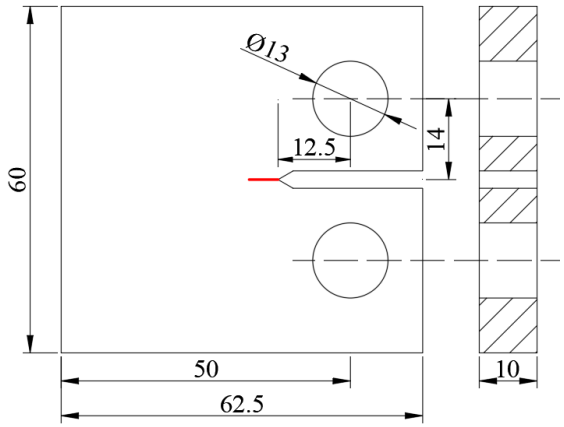


Fig. 4 Dimensions of CT model (unit: mm)

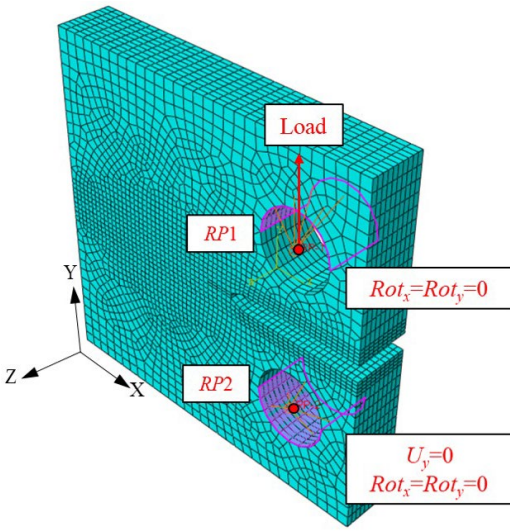


Fig. 5 Boundary conditions of FE model

A user subroutine UMIXMODEFATIGUE supported by ABAQUS was compiled and implemented to define the crack propagation behaviour as shown in Eq. (10)-(11). The cyclic loading was conducted under a stress ratio $R$ of 0.1, 0.5 and 0.9. Fig. 6 illustrates the fatigue crack propagation of CT model under a stress ratio $R$ of 0.1 as an example. The fatigue crack started with an initial length of 17.5 mm at $N$ = 0 and propagated gradually until it reached a final length of 50 mm at $N = 7.1\times10^6$. The crack propagation behaviour was assessed by the SIF of mode I ($K_I$) due to the loading condition of pure tension. The relationship between the crack propagation rate $da/dN$ and the SIF range $\Delta K_I$ calculated based on the FE model is shown in Fig. 7. Besides, the SIF range $\Delta K_I$ of CT model can be calculated using Eq. (12) as proposed by ISO 12108 [43], thus relationship of $da/dN$ to $K_I$ calculated based on the analytical method is also shown in Fig. 7 for comparison. It is observed that the crack propagation rate $da/dN$ calculated by the FE model agrees well with the analytical results under different stress ratios $R$. The simulated $da/dN$ deviates from the analytical results when $\Delta K_I$ is very high and the LEFM no longer works, which is not the condition studied in this research. Above all, the XFEM in combination with VCCT can contribute to favourable

prediction results and is applied in the following analysis of crack propagation.

$$\Delta K_I = \frac{\Delta F\left(2+\frac{a}{W}\right)\left(0.886+4.46\frac{a}{W}-13.32\left(\frac{a}{W}\right)^2+14.72\left(\frac{a}{W}\right)^3-5.6\left(\frac{a}{W}\right)^4\right)}{B\sqrt{W}\left(1-\frac{a}{W}\right)^{1.5}} \tag{12}$$

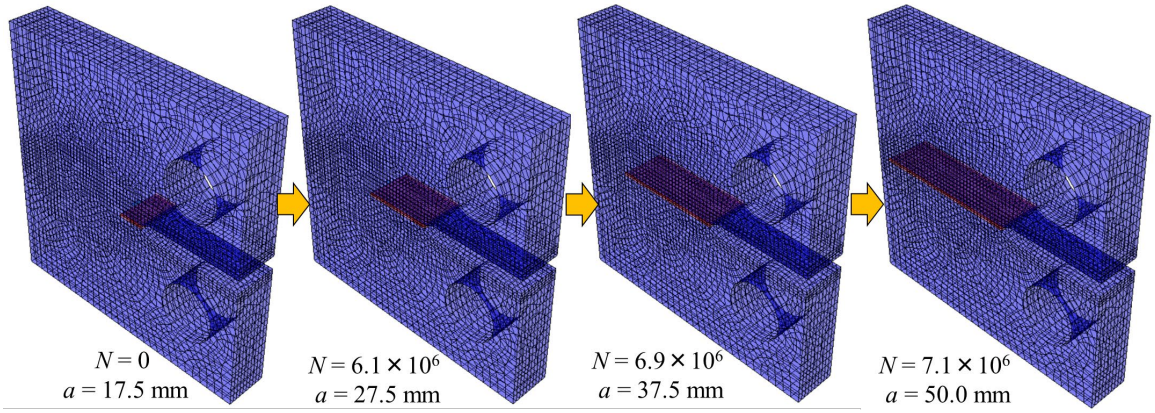


Fig. 6 Crack propagation simulation in combination of XFEM and VCCT

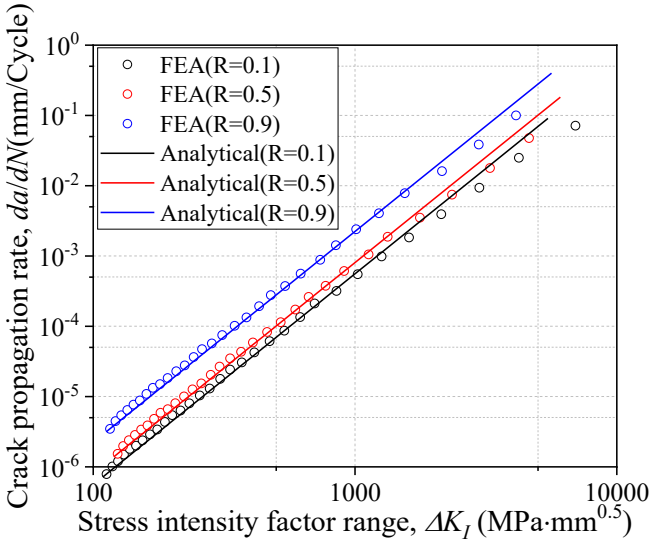


Fig. 7 Comparison of crack propagation rate *da*/*dN* between the simulation and analytical results

## 2.3 Procedures

Fig. 8 indicates the procedure of the proposed method for fatigue life assessment of the out-of-plane gusset welded joints. Firstly, the welding condition, bead geometry and material properties of the steel are collected to assess the residual stress distribution by the thermal-mechanical analysis. The residual stress field is defined as the initial stress for structural analysis. Secondly, the FSS constitutive models of different

welded zones are assigned to the FE model, respectively. The cyclic loading is then applied to the welded joints until the stress-strain response is converged. It should be noted that the welded joints were only divided into WM and BM in this research since the geometric size of HAZ was unavailable. Thirdly, the local strain approach is used to assess the crack initiation life $N_c$ based on the converged stress-strain response. The Smith, Watson and Topper (*SWT*) approach is employed [44] to consider the effects of mean stress on the crack initiation life $N_c$. Finally, the converged stress-strain response is defined as the initial stress for assessment of crack propagation rate by the XFEM and VCCT. The Paris law corrected by mean stress is utilised to calculate the crack propagation life $N_p$. The fatigue failure life $N_f$ is therefore defined as seen Eq. (13).

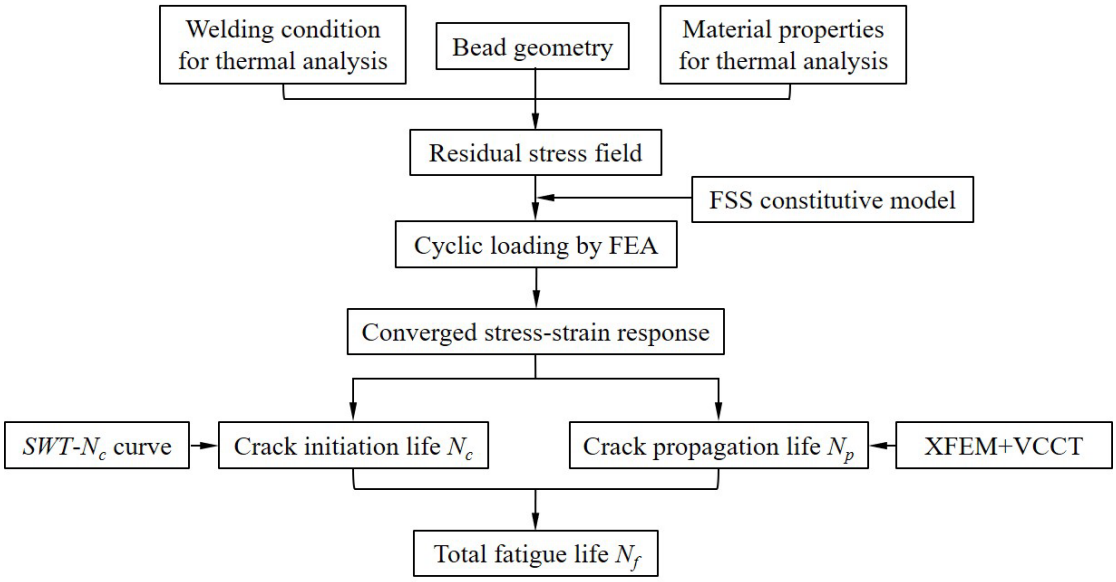


Fig. 8 Procedures for fatigue life assessment of the out-of-plane gusset welded joints

$$N_f = N_c + N_p \tag{13}$$

## 2.4 Review of fatigue tests

The proposed fatigue life assessment method was verified by the fatigue tests of the out-of-plane gusset welded joints previously conducted by the authors [45]. The specimens of the out-of-plane gusset welded joints were made of the Grade 345 steel and joined using the $CO_2$ gas shielded arc welding process. The

joining was conducted by a total of four paths under a welding voltage $U$ of 30.5 V and welding current $I$ of 270 A. The welding speed was controlled by a welding robot at 6.7 mm/s. The specimens were constrained at the welding frame and the subsequent welding path was not conducted until the previous welding path was cooled down to the room temperature. The general geometry and welding paths are shown in Fig. 9. To approximate the real bead shape for the FE model, the bead geometry was measured by a scanning machine and analysed based on the spline model (Fig. 10) as proposed by the authors [18]. The bead geometry of six specimens is listed in Table 2. The fatigue loading was conducted on the specimens at a stress ratio $R$ of 0.05 and frequency of 7 Hz. The fatigue tests results, including the nominal stress range $\Delta\sigma_n$ and fatigue failure life $N_f$, were also shown in Table 2.

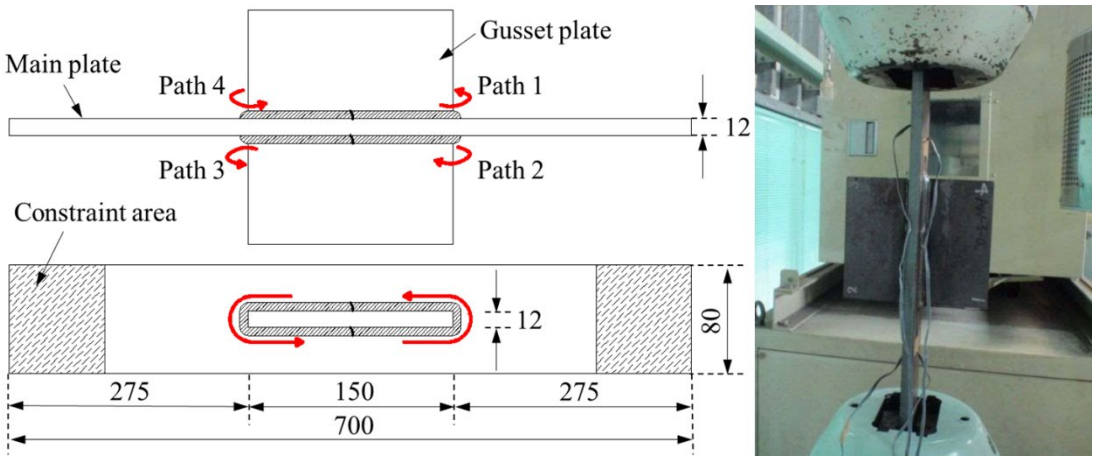


Fig. 9 General geometry, welding condition and loading scenario of out-of-plane gusset welded joints specimens (unit: mm)

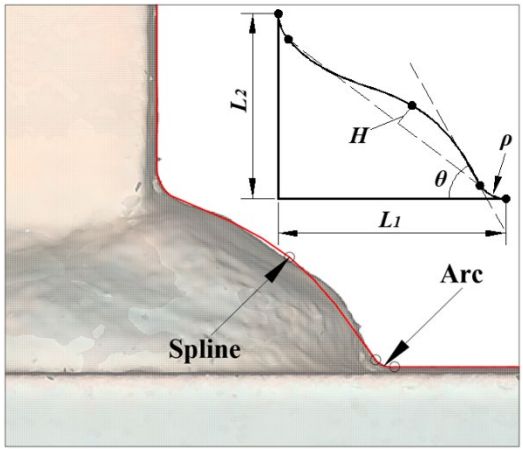


Fig. 10 Spline model for approximation of bead geometry [18]

Table 2 Bead geometry and results of fatigue tests

| Number | $\rho$/mm | $\theta$/° | $L_1$/mm | $L_2$/mm | $H$/mm | $\Delta\sigma_n$/MPa | Fatigue failure life $N_f$/cycle |
|---|---|---|---|---|---|---|---|
| S1 | 0.55 | 60.4 | 10.15 | 8.72 | 0.85 | 150 | 317479 |
| S2 | 0.64 | 74.4 | 9.20 | 8.47 | 0.61 | 80 | 2045000 |
| S3 | 0.67 | 61.1 | 9.92 | 8.59 | 0.61 | 100 | 1052835 |
| S4 | 0.64 | 58.4 | 9.91 | 9.09 | 0.88 | 125 | 541427 |
| S5 | 0.64 | 60.0 | 10.31 | 7.24 | 0.54 | 175 | 198285 |
| S6 | 0.74 | 60.5 | 10.30 | 7.44 | 0.39 | 200 | 145637 |
| Average | 0.65 | 62.5 | 9.97 | 8.26 | 0.65 | - | - |

The fatigue failure of six specimens all occurred at the weld toe of the weld end. Taking the specimen S1 as an example, it is observed in Fig. 11 (a) and (b) that the fatigue crack initiated at the weld toe with high stress concentration, then propagated along the curved weld end and finally penetrated into the base metal. The fatigue cracks at the weld ends of Path 1 and Path 2 were comparatively small, whilst fatigue failure of the specimen S1 was induced by the through-thickness crack at the weld ends of Path 3 and Path 4 as seen Fig. 11 (c). The longer crack at the weld end of Path 3 combined with the shorter one at the weld end of Path 4 when the crack propagated through the plate thickness, resulting in the fatigue failure of the specimen S1. It should be noted that the simulation of crack initiation and propagation in this research only focuses on a single crack from one weld end, because the bead shape, residual stress and loading conditions were assumed to be identical for four weld ends of specimens.

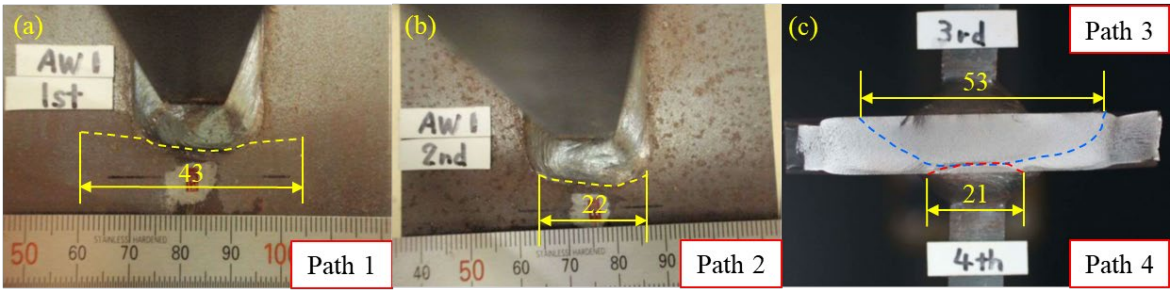


Fig. 11 Fatigue failure of specimen S1 (a) crack growth at the weld end of Path 1 (b) crack growth at the weld end of Path 2 (c) fracture surface at the weld ends of Path 3 and Path 4

## 3 Crack initiation analysis

### 3.1 Simulation of welding residual stress

#### *3.1.1 Thermal analysis*

A sequential coupling method is utilised for simulation of welding residual stress, *i.e.*, the thermal analysis is conducted to obtain the temperature history during the welding process, which serves as the predefined temperature field for the subsequent mechanical analysis. The temperature-dependent thermal and mechanical properties of the Grade 345 steel from [46] were adopted, including the thermal conductivity, specific heat, thermal expansion coefficient, latent heat, density, Young's ratio, Poison's ratio, temperature-dependent elastic-plastic response. The heat convection and radiation during the welding process were considered by defining the convective coefficient of $1.5\times10^{-6}$ J/(s·mm$^2$·°C) and emissivity of 0.85. The process of weld formation was simulated by the method of "element birth and death", by which the bead elements were deactivated first with stiffness matrix decreasing to zero, and then activated following the order of droplet deposition. The double-ellipsoid heat source model [47], which is widely used in simulation of a variety of arc welding techniques, was adopted in this research. The heat source model, including the front and rear quadrant as seen in Fig. 12, is Gaussian distributed and expressed by Eq. (14)-(15).

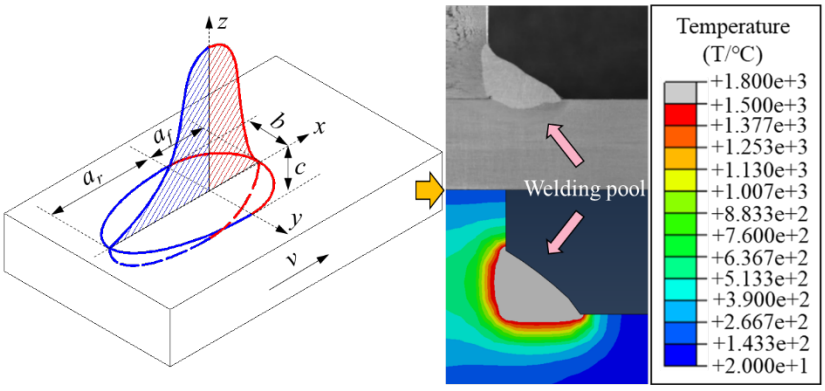


Fig. 12 Double-ellipsoid heat source model and welding pool

$$q_f(x,y,z)=\frac{6\sqrt{3}f_fQ}{\pi a_f bc\sqrt{\pi}}\exp(-3\frac{x^2}{a_f^2}-3\frac{y^2}{b^2}-3\frac{z^2}{c^2}) \quad (14)$$

$$q_r(x,y,z)=\frac{6\sqrt{3}f_rQ}{\pi a_r bc\sqrt{\pi}}\exp(-3\frac{x^2}{a_r^2}-3\frac{y^2}{b^2}-3\frac{z^2}{c^2}) \quad (15)$$

where $Q$ is the effective power of welding and calculated by the product of welding voltage $U$, welding current $I$ and welding efficiency $\eta$; $a_f$, $a_r$, $b$ and $c$ are the half-axial length of the front and rear ellipsoid; $f_f$ and $f_r$ are the energy distribution coefficients of the front and rear ellipsoid and $f_f+f_r=2$. The implementation of the moving heat source model was realised by the user subroutine DFLUX supported by ABAQUS.

The FE model of out-of-plane gusset welded joints was built based on the average bead geometry as listed in Table 2 and shown in Fig. 13. A thermal eight-node solid element DC3D8 was used in the thermal analysis, and a mesh size of 2 mm was determined to ensure the accuracy as suggested by [48]. To be consistent with the real welding condition, the thermal simulation was conducted by the same welding sequence (Path 1 - Path4) with each path followed by the cooling process. The room temperature was defined as 20 ℃ and melting temperature was 1500 ℃. The simulated welding pool is shown in Fig. 12, which shares the similar geometry as the real weld bead. Therefore, it is believed that the simulation process and results of the thermal analysis is adequate.

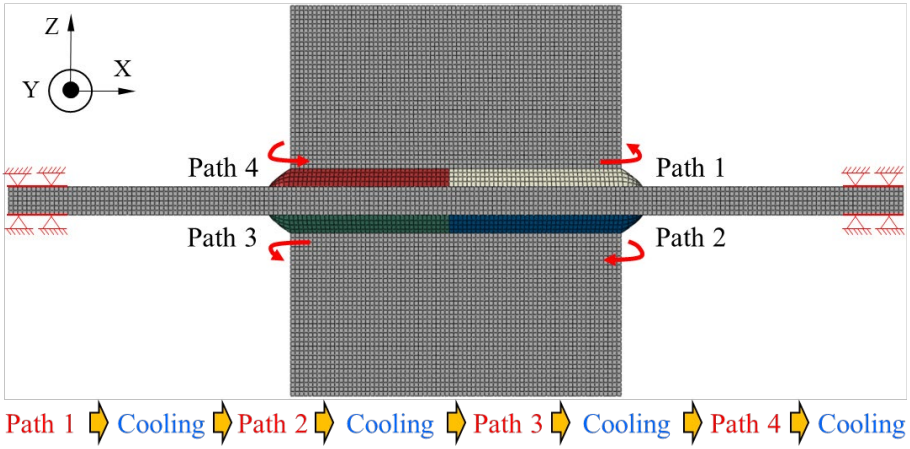


Fig. 13 FE model of out-of-plane gusset welded joints for residual stress simulation by the sequential coupling method

### *3.1.2 Mechanical analysis*

The thermal element was replaced by the mechanical element C3D8, and the temperature history obtained by the thermal analysis served as the heat load on the mechanical analysis. The boundary condition of the structural analysis was decided as seen in Fig. 13 to be consistent with the real welding condition as seen in Fig. 14(a). The validity of the thermal-mechanical analysis was verified by comparing to the measurements of residual stress of the out-of-plane gusset welded joints with similar geometry [26-28, 49-52], though the plate thickness and welding techniques are different in some cases. The residual stress contour of the FE model is shown in Fig. 14(b). The welding residual stress distribution along the transverse and longitudinal direction is reported in Fig. 14(c) and (d).

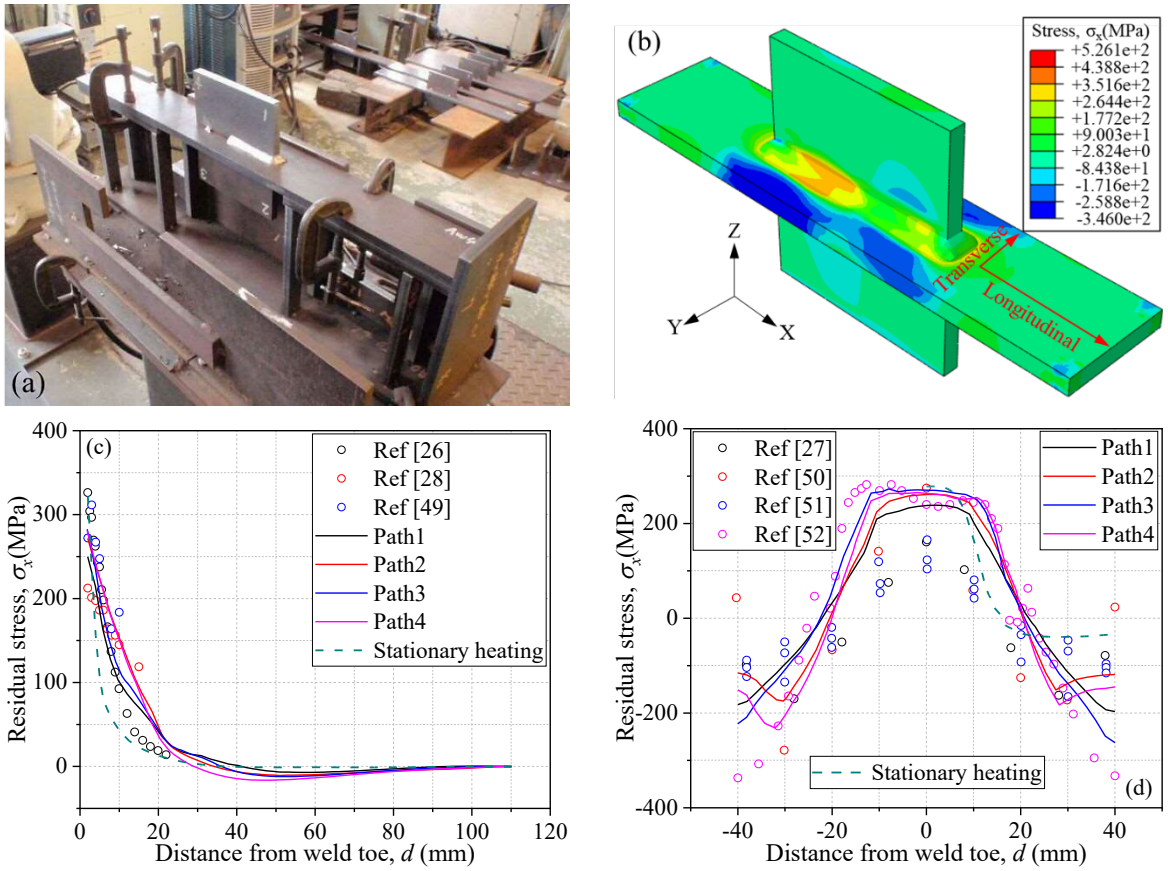


Fig. 14 Simulated welding residual stress of the out-of-plane gusset welded joint by sequential coupling method (a) the boundary condition during the welding process (b) residual stress contour (c) residual stress $\sigma_x$ in the longitudinal direction (d) residual stress $\sigma_x$ in the transverse direction

As seen in Fig. 14(c), the simulated residual stress is tensile and declines rapidly with increasing

distance from the weld toe. The residual stress distribution of four paths, though slightly different due to the welding sequence, illustrates close values and trend as a whole. The measured residual stress from [26] was the average of four paths, whilst those from [28] and [49] were not specified. Nonetheless, the simulated residual stress agrees well with the measurements. Fig. 14(d) shows the residual stress distribution in the transverse direction, and the maximum tensile residual stress is found at the weld toe for both simulation and measurement. It is illustrated that there are no significant differences between simulated residual stress distribution of four paths, and the simulated results are also in good agreement with the measurements. It is noted that there is an inflection point of residual stress at about ± 30 mm for Path 2 and Path 4, which is not observed for Path 1 and Path 3. The same inflection point is also observed in [27] and [50], which is not the case for [51] and [52]. A possible explanation for this phenomenon is that the shrinkage of subsequently welded Path 2 and Path 4 during the cooling process is counteracted by the residual deformation of previous welding Path 1 and Path 3, which results in the decreasing of compressive residual stress far from the weld toe. One possible reason for the different residual stress distributions in the references is that the measurements were conducted on different sides of the out-of-plane gusset welded joints.

*3.1.3 Stationary heating analysis*

The sequential coupling method for welding residual stress simulation can have a high computational cost, especially for the structural discontinuities such as the weld toe, which requires local mesh refinement to ensure the accuracy of structural analysis. The stationary heating method, a simplified procedure versus the sequential coupling method, is computationally efficient and obtains the almost equivalent accuracy of residual stress simulation at the same time. In this research, the stationary heating analysis was also conducted by a quarter symmetry model of gusset welded joints. The same material parameters were used as in the sequential coupling method. The heating temperature was decided to be 800 ℃ as referred to [28]

285 to give accurate results compared to the measurements and the sequential coupling method. The elements in
286 the vicinity of the weld toe were refined to 0.1 mm, so that local residual stress at the weld toe with high
287 accuracy could be obtained for the subsequent cyclic elastoplasticity analysis. Furthermore, the mesh size
288 was transited from 0.1 mm to 1 mm for the crack propagation analysis. The FE model of the stationary
289 heating analysis is shown in Fig. 15(a). During the simulation, Path 1 was first heated up to 800 ℃ and then
290 cooled down to room temperature, followed by heating and cooling of Path 2. The welding residual stress
291 contour is illustrated in Fig. 15(b). Compared to the sequential coupling method as seen in Fig. 14(b), the
292 peak value of welding residual tensile stress and compressive stress simulated by the stationary heating
293 method are both higher. The transverse and longitudinal residual stress along the same paths are also reported
294 in Fig. 14(c) and (d). It is observed that the decline rate of longitudinal residual stress simulated by the
295 stationary heating method is higher than that by the sequential coupling method due to the limited heating
296 region, whilst it still has a good agreement with the measurement. The transverse residual stress also follows
297 a similar distribution as the measurement. Although the compressive residual stress far from the weld toe is
298 smaller than that simulated by the sequential coupling method, it is still located among the measured points.
299 Above all, the welding residual stress simulated by the stationary heating method have favourable accuracy,
300 thus the quarter symmetry FE model and simulated residual stress are used in the following elastoplasticity
301 analysis and crack propagation analysis.

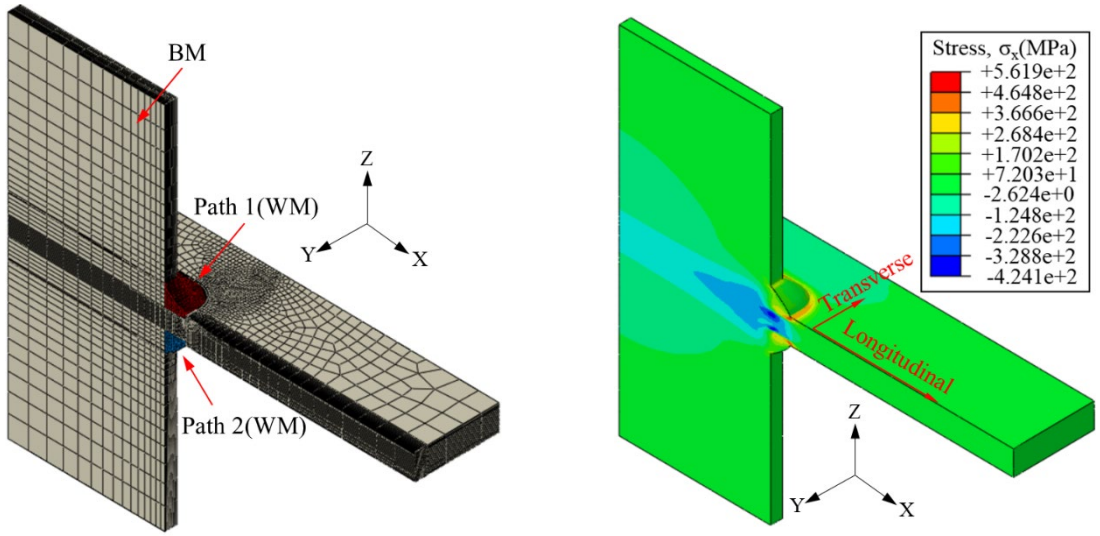


Fig. 15 Simulated welding residual stress of the gusset welded joint by stationary heating method (a) the quarter symmetry FE model (b) welding residual stress contour

302

303 3.2 Cyclic elastoplasticity response

304 The fatigue crack initiation life $N_c$ is often suggested to be assessed by the local strain method
305 considering the influence of mean stress, stress concentration and welding residual stress. The stress-strain
306 relationship at the hysteresis stabilization is critical for the accurate prediction of crack initiation life $N_c$. In
307 this research, the FSS constitutive model was used to assess the converged stress-strain relationship in the
308 high cycle fatigue regime. The FE model was divided into BM and WM, as shown Fig. 15(a). The
309 corresponding material properties, as summarised in Table 1, were assigned. The welding residual stress in
310 Fig. 15(b) was defined as the initial stress, and the cyclic loading following the same loading condition in
311 the fatigue experiment (Table 1) was conducted on the quarter symmetry model of the out-of-plane gusset
312 welded joints. Fig. 16 shows the local stress-strain response of the weld toe in the first 50 cycles.

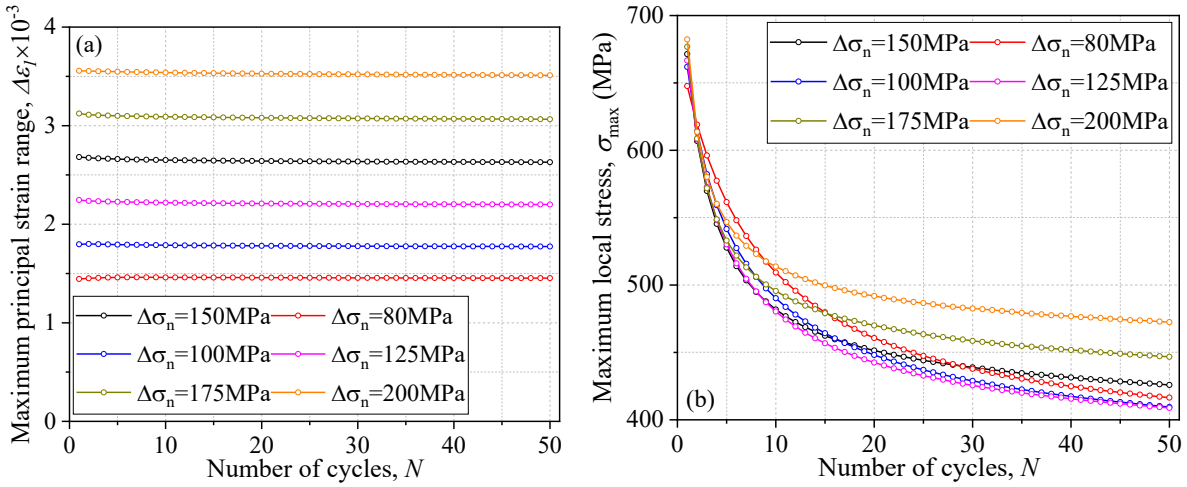


Fig. 16 Variation of strain ranges and stresses in the first 50 cycles: (a) Maximum principal strain range $\Delta\varepsilon_1$; (b) Maximum local stress $\sigma_{max}$

As seen in Fig. 16(a), the variation of the maximum principal strain range $\Delta\varepsilon_1$ of six specimens only occurs in a few cycles and no significant change is observed afterwards, indicating the rapid convergence of $\Delta\varepsilon_1$. The cyclic softening is illustrated for all six specimens, and the trend to convergence of the maximum local stress $\sigma_{max}$ can be achieved before Cycle 50, as shown in Fig. 16(b), whilst the specimens under lower local stress ranges $\Delta\sigma_n$ show a slower convergence rate. The stress-strain relationship at Cycle 50 was used for predicting the fatigue crack initiation life $N_c$ and subsequent fatigue crack propagation life $N_p$ due to the hysteresis stabilization.

### 3.3 Crack initiation life prediction

The *SWT* approach was used for predicting the fatigue crack initiation, considering the effects of the stress ratio $R$. The *SWT* parameter in this research was defined by the product of the maximum principal strain range $\Delta\varepsilon_1/2$, and the maximum local stress $\sigma_{max}$ sharing the same direction as $\varepsilon_1$. The authors previously collected the experimental data for the Grade 345 steel ($R$ = -1) and established the relationship of *SWT* to crack initiation life $N_c$, as shown in Eq. (16)-(17) and Fig. 17 [20].

$$\Delta\varepsilon_1 = 2.23N_c^{-0.8475} + 0.026N_c^{-0.1719} \tag{16}$$

$$SWT = \frac{\Delta\varepsilon_1}{2}\cdot\sigma_{max} = 1506.68N_c^{-0.9805} + 5.29N_c^{-0.1994} \tag{17}$$

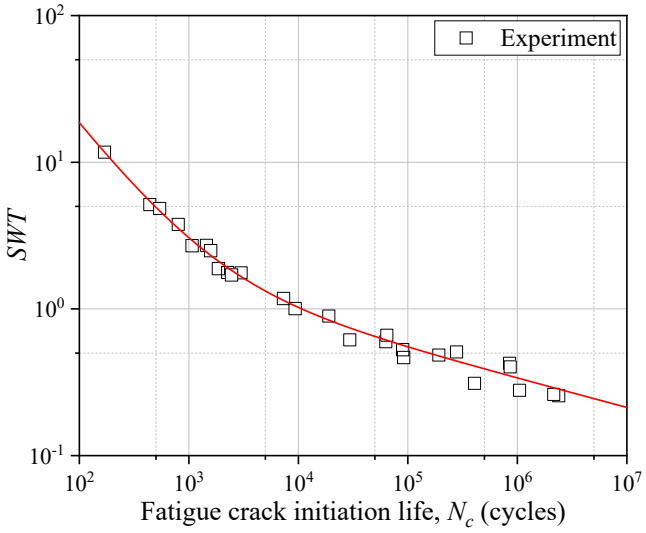


Fig. 17 Fatigue crack initiation life $N_c$ curve of the Grade 345 steel based on *SWT* parameter [20]

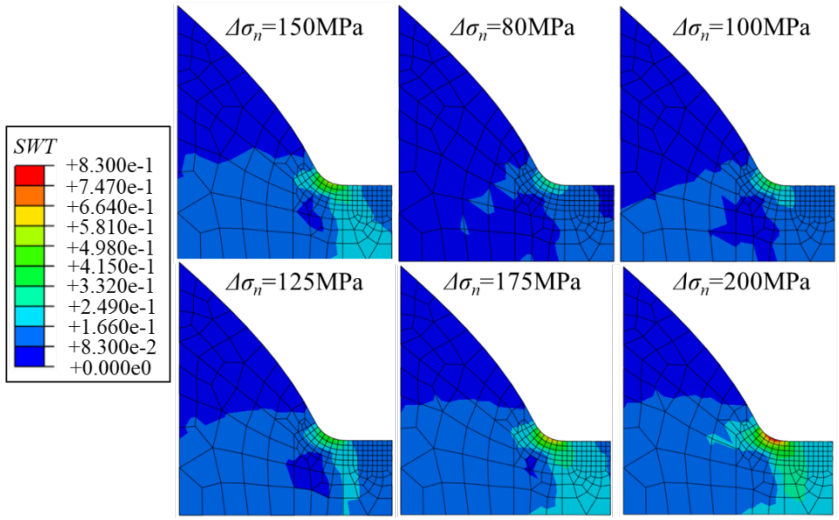


Fig. 18 *SWT* contour at the weld toe of out-of-plane gusset welded joints

Based on the converged stress-strain response at $N = 50$, as simulated in Section 3.2, the *SWT* parameter of elements near the weld toe was calculated to identify the node with the maximum *SWT* for crack initiation life $N_c$ prediction. Fig. 18 shows the *SWT* contours of six specimens. The crack initiation life $N_c$ of six specimens was then predicted by the node with the maximum *SWT* parameter and summarised in Table 3.

Table 3 Fatigue crack initiation life $N_c$ assessed by the *SWT* parameter

| Specimen | Maximum principal strain range $\Delta\varepsilon_1\times10^{-3}$ | Maximum local stress $\sigma_{max}$/MPa | *SWT* | Fatigue crack initiation life $N_c$/cycle |
|---|---|---|---|---|
| 1 | 2.629 | 426 | 0.560 | 94000 |
| 2 | 1.453 | 416 | 0.303 | 1750000 |
| 3 | 1.774 | 410 | 0.363 | 700000 |
| 4 | 2.200 | 409 | 0.450 | 255000 |
| 5 | 3.065 | 447 | 0.685 | 40200 |

| | | | | |
|---|---|---|---|---|
| 6 | 3.511 | 473 | 0.830 | 19600 |

## 4 Crack propagation analysis

### 4.1 Crack propagation behaviour

The fatigue crack propagation life $N_p$ was estimated based on the XFEM in combination with VCCT. The Paris law for the mixed-mode crack, as explained in Section 2.2, was used to describe the relationship between the fatigue crack propagation rate $da/dN$ and the equivalent SIF range $\Delta K_{eq}$. It should be noted that the welding residual stress was relaxed during the cyclic loading, thus the converged stress-strain response at Cycle 50 was defined as the initial state for crack propagation life $N_p$ assessment. An initial crack was embedded into the weld toe of the FE model at the position that had the maximum $SWT$ parameter. The initial crack aspect ratio was assumed to be 1.0 as recommended in many references [53-54], indicating a semi-circular crack shape. The initial crack depth was assumed to be 0.5 mm, because the $SWT$- $N_c$ curve in Fig. 17 to predict the crack initiation life $N_c$ corresponded to the surface crack length of 0.5 mm - 1 mm [20]. Since there was no evident inflection of crack during the propagation process in the fatigue experiment as seen in Fig. 11 (a), the fatigue crack was assumed to propagate perpendicular to the loading direction. The crack propagation of specimen S2 under the nominal stress range of $\Delta\sigma_n$ = 80 MPa is shown in Fig. 19 as an example.

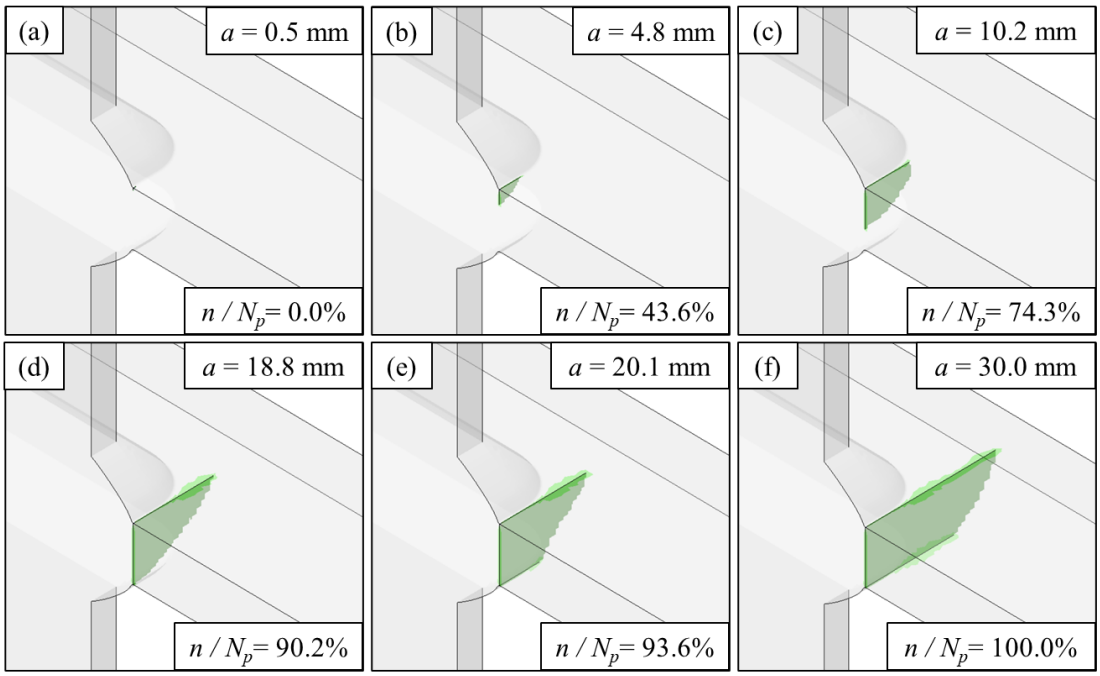


Fig. 19 Fatigue crack propagation simulated by XFEM and VCCT ($\Delta\sigma_n$ = 80 MPa)

As explained in Section 2.4, it is assumed that the fatigue crack only initiates from one side of the weld end. The surface crack length $a$ corresponding to the loading cycles $n$ is also illustrated in each figure. It is observed that the crack initiates from the weld end by the assumed quadrant arc (Fig. 19 (a)). The crack shape gradually becomes elliptical as seen Fig. 19 (b) which follows the real crack shape in the experiment, indicating a higher propagation rate in the surface direction than in the depth direction. The crack propagation at the weld end accounts for most of the crack propagation life ($n$ / $N_p$ = 74.3%) as seen Fig. 19 (c). The through- thickness crack is observed at $n$ / $N_p$ = 90.2% (Fig. 19 (d)) and the crack propagation is accelerated by a trapezoid shape (Fig. 19 (e)). The crack propagation life $N_p$ is defined by the surface crack length $a$ = 30.0 mm (Fig. 19 (f)), because the increase of crack propagation life $N_p$ converges as discussed in Section 4.2.

## 4.2 Crack propagation life prediction

Based on the equivalent stress intensity factor $K_{eq}$ which considers the influence of mixed-mode cracks, the crack propagation rate $da/dN$ was calculated by Eq. (10). Fig. 20 summarises the curves of crack length

$a$ to number of cycles $N$ of six specimens. It is obvious that the specimen loaded by higher nominal stress range $\Delta\sigma_n$ has a longer propagation life $N_p$. The crack propagation rate slows down and zigzags are observed when crack length $a$ reached about 6.0 mm. The temporary decrease of crack propagation rate can be explained by the fact that the crack has propagated away from the weld toe with high stress concentration, thus the influence of weld magnification on the SIF due to structural discontinuities is reduced. The zigzags of crack propagation result from the mesh transition from smaller size to larger size, as the element size becomes irregular and several elements are involved in the cracking path. The fatigue crack propagation life $N_p$ is defined by the crack length $a$ = 30.0 mm when the increase of $N_p$ converges, thus the fatigue failure life $N_f$ can be predicted by Eq. (13) and illustrated in Fig. 21. To confirm the accuracy of the proposed method, the experimental results were also added for comparison.

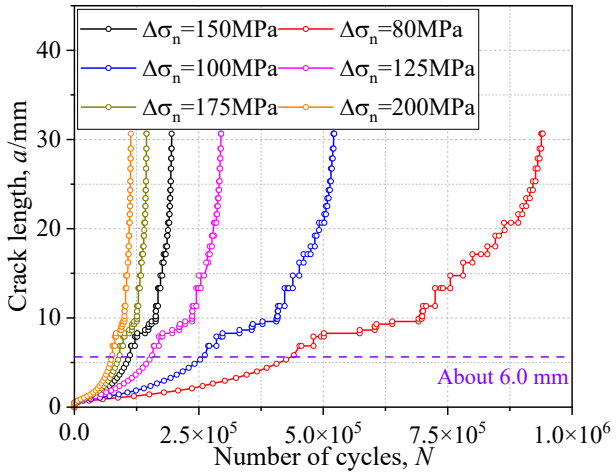


Fig. 20 Relationship of crack length to number of cycles of six specimens

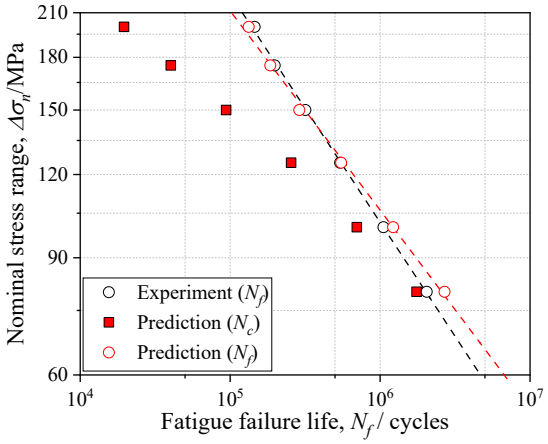


Fig. 21 Comparison of the fatigue failure life $N_f$ between the prediction and experiment results

Although there is no record of the crack initiation life $N_c$ in the experiments, the fatigue failure life $N_f$ in the FE model agrees well with the experimental results. This indicates that the proposed method can predict the fatigue life of out-of-plane gusset welded joints with high accuracy under the current welding and loading condition. The prediction of fatigue failure life $N_f$ is better for the middle-cycle fatigue regime, though the fatigue life is overestimated for the high-cycle fatigue regime. The data points of predicted fatigue

failure life $N_f$ fit well with a *R-square* of 0.997, whilst the slope of the *S-N* curve by the proposed prediction method deviates from the experiment results. Thus, a further improvement of accuracy of the proposed method can include the modification of material constants used in predicting crack initiation and propagation life based on the fatigue tests of the materials.

## 5 Discussion

### 5.1 Mean stress effects

The *SWT* parameter (Eq. (17)) and Walker's equation (Eq. (11)) were used to predict the crack initiation life $N_c$ and crack propagation life $N_p$ with correction of mean stress in this research. However, the influence of mean stress on fatigue life prediction of out-of-plane gusset welded joints is not yet clarified. Therefore, the prediction of fatigue life without mean stress correction was also conducted for comparison. The crack initiation life $N_c$ without mean stress correction can be predicted by the local strain approach (Eq. (16)), as shown in Fig. 22(a). It is observed that the crack initiation life $N_c$ is significantly overestimated without mean stress correction. This is because the $\Delta\varepsilon_1$ - $N_c$ relationship of S355 steel (Eq. (16)) is established based on the fatigue experiment under the fully reversed loading ($R$ = -1). The fatigue damage should be corrected before Eq. (16) can be used for the loading condition in this research ($R$ = 0.05).

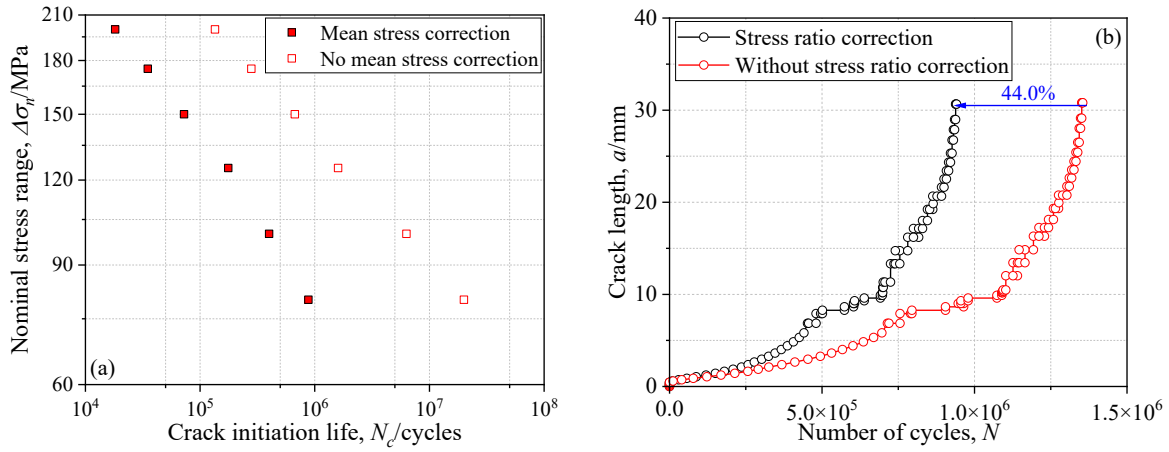


Fig. 22 Influence of mean stress on fatigue life prediction (a) crack initiation life $N_c$ (b) crack propagation life $N_p$

The crack propagation life $N_p$ without mean stress correction can be predicted by the Paris law, neglecting the correction parameter $\gamma$ in Eq. (11). Taking the loading condition of specimen S2 ($\Delta\sigma_n$ = 80 MPa) as an example, Fig. 22(b) shows the crack length $a$ - number of cycles $N$ curves with and without mean stress correction. The crack propagation life $N_p$ is overestimated by 44.0% if the influence of mean stress is neglected. Therefore, mean stress correction is necessary in both prediction of the crack initiation life $N_c$ and crack propagation life $N_p$ of the out-of-plane gusset welded joints for high accuracy.

## 5.2 Mixed-mode crack effects

The stress intensity factors $K$ of mode I, mode II and mode III of specimen S2 ($\Delta\sigma_n$ = 80 MPa) under the cyclic loading were collected in Fig. 23. It is observed that the crack propagation of the out-of-plane gusset welded joints under tension loading is dominated by the mode I, and both $K_{II}/K_I$ and $K_{III}/K_I$ are smaller than 30%. Taking the loading condition of specimen S2 ($\Delta\sigma_n$ = 80 MPa) as an example, the crack propagation life $N_p$ was also predicted by SIF $K_I$ instead of the equivalent SIF $K_{eq}$. Fig. 24 illustrates the predicted crack length $a$ - number of cycles $N$ curves with and without mixed-mode crack correction, and it shows that there is little difference (3.3%) between the two conditions. This is reasonable because the SIFs of mode II and mode III are too small to have significant influence on the crack propagation. The effects of mixed-mode crack might be more significant for the welded joints under complex loading conditions.

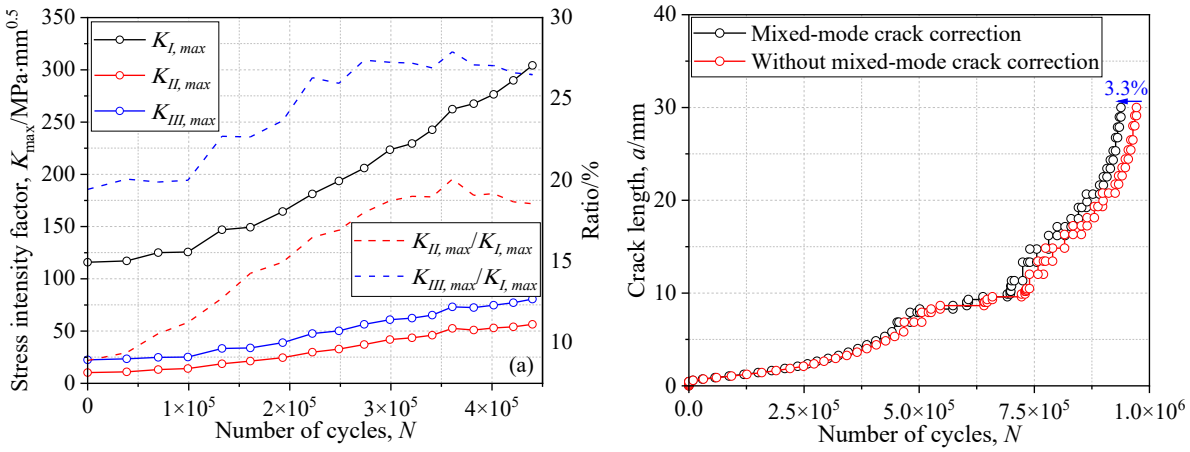

Fig. 23 Stress intensity factor SIFs of crack mode I, II and III

Fig. 24 Influence of mixed-mode crack on crack propagation life prediction

407

408 5.3 Residual stress effects

409 The influence of residual stress on the fatigue crack propagation life $N_p$ is often considered by defining
410 the welding residual stress as the initial stress for $N_p$ prediction [28,55-56]. It should be noted that the welding
411 residual stress is gradually relaxed under the cyclic loading, and finally converges to a stress state that is
412 quite different from the original welding residual stress after a certain number of cycles [25]. Therefore, the
413 residual stress that influences the crack propagation rate is actually the converged stress state during the
414 cyclic loading, instead of the initial welding residual stress. Taking the loading condition of specimen S2
415 ($\Delta\sigma_n$ = 80 MPa) as an example, Fig. 25 shows the curves of crack length $a$ to number of cycles $N$ under no
416 residual stress, welding residual stress and converged cyclic stress.

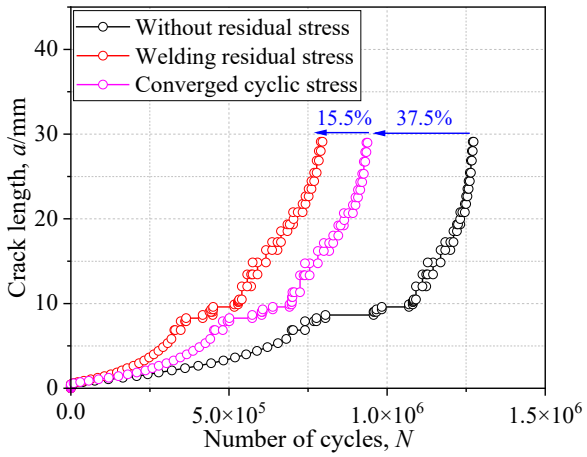


Fig. 25 Influence of residual stress on crack propagation life prediction

417 It is observed that the crack propagation life $N_p$ without considering residual stress (black curve) is
418 highly overestimated and shows a difference of 37.5%, as the higher mean stress resulted from the residual
419 stress is neglected. The crack propagation life $N_p$ considering the welding residual stress (red curve) is shorter
420 than that considering the converged stress (pink curve) and shows a difference of 15.5%. This is reasonable
421 because the welding residual stress is relaxed during the cyclic loading, resulting in a lower mean stress. As

there is a noticeable difference between the predicted crack propagation life $N_p$ with and without considering the relaxation of welding residual stress, it is suggested to predict the crack propagation life $N_p$ by the converged stress under the cyclic loading to ensure the accuracy.

## 6 Conclusions and future work

In the present study, a fatigue life assessment approach for out-of-plane gusset welded joints was proposed, using the FSS constitutive model to describe the local cyclic elastoplasticity and the XFEM method to analyse the crack propagation behaviour. Considering the influence of welding residual stress simulated by the thermal-mechanical analysis, the crack initiation life was predicted by a local strain approach using an *SWT* parameter for mean stress correction. Defining the converged cyclic stress-strain response as the initial state for crack propagation analysis, the Walker's equation and equivalent SIF were used to predict the crack propagation life with mean stress and mixed-mode crack correction. The predicted fatigue failure life agreed well with the experimental results, indicating the favourable performance of the proposed approach to assess the fatigue life of out-of-plane gusset welded joints under the current welding and loading conditions.

The cyclic stress-strain response of Grade 345 steel was well assessed by the novel FSS constitutive model in both macroscopic and sub-yield stress state. The satisfactory accuracy of XFEM in combination with VCCT to predict the crack propagation rate was verified by a CT model under a wide range of stress ratios. The sequential coupling method was initially applied to simulate the welding residual stress with favourable results compared to the measurements, whilst it had a high computational cost and was not suitable for the following cyclic loading analysis that required local mesh refinement. Therefore, the simulated welding residual stress by the stationary heating method with comparable accuracy was recommended.

The influence of mean stress, mixed-mode crack and residual stress on crack initiation and propagation life was also discussed. Both crack initiation life and propagation life were significantly overestimated without mean stress correction. The crack propagation of out-of-plane gusset welded joints under tension loading was dominated by the crack mode I, thus the mixed-mode crack had limited influence on the crack propagation life. Due to the relaxation of welding residual stress, the crack propagation life was underestimated by 15.5% if only the initial welding residual stress was considered, whilst the crack propagation life was highly overestimated by 37.5% without considering residual stress. Therefore, it was suggested to predict the crack propagation life by the converged stress under the cyclic loading to ensure the accuracy.

The present study shows the fatigue life prediction of out-of-plane gusset welded joints under tension loading, whilst further investigation should be conducted on its application to more complex loading conditions. Possible improvement of accuracy of the proposed method can include the modification of material constants used in predicting crack initiation and propagation life based on the fatigue tests of the WM, HAZ and BM. The multi-cracks as observed in the fatigue experiment should also be considered to include the influence of simultaneous crack propagation.

## Acknowledgements

The authors gratefully acknowledge the support from the Departmental Postdoctoral Fellowship Scheme, Department of Civil and Environmental Engineering, The Hong Kong Polytechnic University and The Chinese National Engineering Research Centre for Steel Construction (Hong Kong Branch) at The Hong Kong Polytechnic University.

## Reference

[1] X. Qiang, Y. Wu, Y. Wang, J. Xu, Novel crack repair method of steel bridge diaphragm employing Fe-SMA, *Eng.*

*Struct.* 292 (2023) 116548. https://doi.org/10.1016/j.engstruct.2023.116548.

[2] L. Fang, Z. Fu, B. Ji, S. Kainuma, Research on mixed mode crack drilling under out-of-plane shear in steel bridge deck, *Int. J. Fatigue* 156 (2022) 106679. https://doi.org/https://doi.org/10.1016/j.ijfatigue.2021.106679.

[3] S. Wang, J. He, Y. Liu, Shear behavior of steel I-girder with stiffened corrugated web, Part I: Experimental study, *Thin-Walled Struct.* 140 (2019) 248-262. https://doi.org/10.1016/j.tws.2019.02.025.

[4] R. Connor, J. Fisher, Identifying effective and ineffective retrofits for distortion fatigue cracking in steel bridges using field instrumentation, *J. Bridg. Eng.* 11 (6) (2006) 745-752. https://doi.org/10.1061/(asce)1084-0702(2006)11:6(745).

[5] Y. Wang, B. Ji, Z. Fu, Y. Yao, Fatigue repairing craftsmanship of deck-to-vertical stiffener weld in the steel bridge deck, *Adv. Steel Constr.* 15 (3) (2019) 232-241. https://doi.org/10.18057/IJASC.2019.15.3.3.

[6] K. Yamada, T. Ishikawa, T. Kakiichi, Rehabilitation and improvement of fatigue life of welded joints by ICR treatment, *Adv. Steel Constr.* 11 (3) (2015) 294-304. https://doi.org/10.18057/IJASC.2015.11.3.4.

[7] K. Kyung, J. Park, S. Jun, J. Kim, A study of the evaluation of fatigue crack at welded joint for steel plate girder, *Procedia Eng.* 14 (2011) 1543-1548. https://doi.org/10.1016/j.proeng.2011.07.194.

[8] C. Wang, Y. Wang, B. Cui, L. Duan, N. Ma, J. Feng, Numerical simulation of distortion-induced fatigue crack growth using extended finite element method, *Struct. Infrastruct. Eng.* 16 (1) (2020) 106-122. https://doi.org/10.1080/15732479.2019.1650076.

[9] F. Xu, W. Pan, T. Chan, T. Sheehan, L. Gardner, Fracture prediction for square hollow section braces under extremely low cycle fatigue, *Thin-Walled Struct.* 171 (2022) 108716. https://doi.org/10.1016/j.tws.2021.108716.

[10] F. Xu, T. Chan, T. Sheehan, L. Gardner, Prediction of ductile fracture for circular hollow section bracing members under extremely low cycle fatigue, *Eng. Struct.* 214 (2020) 110579. https://doi.org/10.1016/j.engstruct.2020.110579.

[11] J. Schijve, Fatigue of structures and materials, Springer, 2001. https://doi.org/10.1007/0-306-48396-3.

[12] S. Maddox, Fatigue strength of welded structures, Woodhead Publishing, 1991. https://doi.org/10.1016/C2013-0-17455-7.

[13] M. Yang, B. Ji, Z. Yuanzhou, Z. Fu, Fatigue behavior and strength evaluation of vertical stiffener welded joint in orthotropic steel decks, *Eng. Fail. Anal.* 70 (2016) 222-236. https://doi.org/10.1016/j.engfailanal.2016.05.001.

[14] C. Wang, Y. Wang, L. Duan, D. Wouter, Distortion-induced fatigue behavior of vertical stiffener web gaps in steel girder bridges, *Thin-Walled Struct.* 180 (2022) 109892. https://doi.org/doi.org/10.1016/j.tws.2022.109892.

[15] Y. Ono, C. Baptista, K. Kinoshita, H. Yıldırım, A. Nussbaumer, A reanalysis of fatigue test data for longitudinal welded gusset joints in as-welded and high frequency mechanical impact (HFMI)-treated state, *Int. J. Fatigue* 149 (2021) 106167. https://doi.org/10.1016/j.ijfatigue.2021.106167.

[16] N. Yamamoto, M. Mouri, T. Okada, M. Takeshi, An analytical and experimental study on the thickness effect of fatigue strength in large-scale-welded models, *Weld World* 58 (2014) 329-337. https://doi.org/10.1007/s40194-014-0118-y.

[17] W. Park, C. Miki, Fatigue assessment of large-size welded joints based on the effective notch stress approach, *Int. J. Fatigue* 30 (9) (2008) 1556-1568. https://doi.org/10.1016/j.ijfatigue.2007.11.012.

[18] Y. Wang, Y. Luo, Y. Kotani, S. Tsutsumi, Generalized SCF formula of out-of-plane gusset welded joints and assessment of fatigue life extension by additional weld, *Materials.* 14 (5) (2021) 1-23. https://doi.org/10.3390/ma14051249.

[19] T. Shiratsuchi, N. Osawa, Fatigue life prediction for 9%Ni steel butt welded joints, *Int. J. Fatigue* 142 (2021) 105925. https://doi.org/10.1016/j.ijfatigue.2020.105925.

[20] Y. Wang, R. Fincato, K. Morita, Q. Wang, S. Tsutsumi, Cyclic elastoplasticity-based life assessment of fatigue crack initiation and subsequent propagation in rib-to-deck welded joints, *Int. J. Fatigue* 173 (2023) 107679. https://doi.org/10.1016/j.ijfatigue.2023.107679.

[21] S. Tsutsumi, A. Buerlihan, R. Fincato, Y. Kotani, T. Tsuyama, Numerical study for the effect of shape of additional weld on fatigue strength in out-of-plane gusset welded joint, *Q. J. Japan Weld. Soc.* 38 (2) (2020) 163s-167s. https://doi.org/10.2207/qjjws.38.163s.

[22] R. Sheng, Y. Liu, Y. Yang, R. Hao, A. Chen, Fatigue tests and analysis on welded joints of weathering steel, *Materials.* 15 (19) (2022) 6974. https://doi.org/10.3390/ma15196974.

[23] D. Choi, H. Choi, Fatigue life prediction of out-of-plane gusset welded joints using strain energy density factor approach, *Theor. Appl. Fract. Mech.* 44 (1) (2005) 16-26. https://doi.org/10.1016/j.tafmec.2005.05.002.

[24] K. Gotoh, T. Niwa, Y. Anai, Fatigue crack growth behaviour of an out-of-plane gusset welded joints under biaxial tensile loadings with different phases, *Procedia Mater. Sci.* 3 (2014) 1536-1541. https://doi.org/10.1016/j.mspro.2014.06.248.

[25] J. Hensel, T. Nitschke-pagel, K. Dilger, Effects of residual stresses and compressive mean stresses on the fatigue strength of longitudinal fillet-welded gussets, *Weld World* 60 (2016) 267-281. https://doi.org/10.1007/s40194-015-0284-6.

[26] J. Hensel, T. Nitschke-Pagel, K. Dilger, On the effects of austenite phase transformation on welding residual stresses in non-load carrying longitudinal welds, *Weld World* 59 (2015) 179-190. https://doi.org/10.1007/s40194-014-0190-3.

[27] S. Kainuma, K. To, D. Uchida, N. Yagi, H. Kubo, Fatigue behaviour of out-of-plane gusset joints with one-side fillet weld, 29 (12) (2015) 913-921. https://doi.org/10.1080/09507116.2014.921082.

[28] D. Tchuindjang, W. Fricke, M. Vormwald, Numerical analysis of residual stresses and crack closure during cyclic loading of a longitudinal gusset, *Eng. Fract. Mech.* 198 (2018) 65-78. https://doi.org/10.1016/j.engfracmech.2017.08.018.

[29] P. Paris, F. Erdogan, A critical analysis of crack propagation laws, *J. Fluids Eng. Trans. ASME* 85 (4) (1963) 528-533. https://doi.org/10.1115/1.3656900.

[30] S. Tsutsumi, R. Fincato, Cyclic plasticity model for fatigue with softening behaviour below macroscopic yielding, *Mater. Des.* 165 (2019) 107573. https://doi.org/10.1016/j.matdes.2018.107573.

[31] K. Hashiguchi, On the loading criterion, *Int. J. Plast.* 10 (8) (1994) 871-878. https://doi.org/10.1016/0749-6419(94)90018-3.

[32] S. Tsutsumi, M. Toyosada, K. Hashiguchi, Extended subloading surface model incorporating elastic boundary concept, *J. Appl. Mech.* 9 (2006) 455-462. https://doi.org/10.2208/journalam.9.455.

[33] R. Fincato, T. Yonezawa, S. Tsutsumi, Numerical modeling of cyclic softening/hardening behavior of carbon steels from low- to high-cycle fatigue regime, *Arch. Civ. Mech. Eng.* 23 (2023) 164. https://doi.org/10.1007/s43452-023-00698-4.

[34] K. Morita, M. Mouri, B. Ayang, R. Fincato, S. Tsutsumi, Cyclic elasto-plasticity behavior and fatigue crack initiations lives of low carbon steels and their simulated HAZ, *J. Japan Weld. Eng. Soc.* 40 (1) (2022) 36-43. https://doi.org/10.2207/qjjws.40.36. (in Japanese)

[35] T. Belytschko, T. Black, Elastic crack growth in finite elements with minimal remeshing, *Int. J. Numer. Methods Eng.* 45 (5) (1999) 601-620. https://doi.org/10.1002/(SICI)1097-0207(19990620)45:5<601::AID-NME598>3.0.CO;2-S.

[36] A. Bergara, J. Dorado, A. Martin-Meizoso, J. Martínez-Esnaola, Fatigue crack propagation in complex stress fields: Experiments and numerical simulations using the Extended Finite Element Method (XFEM), *Int. J. Fatigue* 103 (2017) 112-121. https://doi.org/10.1016/j.ijfatigue.2017.05.026.

[37] K. Shivakumar, P. Tan, J. Newman, A virtual crack-closure technique for calculating stress intensity factors for cracked three dimensional bodies, *Int. J. Fract.* 36 (1988) 43-50.

[38] S. Forth, W. Keat, L. Favrow, Experimental and computational investigation of three-dimensional mixed-mode fatigue, *Fatigue Fract. Eng. Mater. Struct.* (25) (2002) 3-15. https://doi.org/10.1046/j.1460-2695.2002.00413.x.

[39] K. Walker, The effect of stress ratio during crack propagation and fatigue for 2024-T3 and 7075-T6 aluminum, *Effects of Environment and Complex Load History on Fatigue Life*, ASTM International, 1970.

[40] A. Hobbacher, Recommendations for Fatigue Design of Welded Joints and Components, Springer, 2016. https://doi.org/10.1007/978-3-319-23757-2.

[41] H. Xin, J. Liu, J. Correia, F. Berto, M. Veljkovic, G. Qian, Mixed-mode fatigue crack propagation simulation by means of Geq and walker models of the structural steel S355, *Theor. Appl. Fract. Mech.* 123 (2023)

https://doi.org/10.1016/j.tafmec.2022.103717.
[42] H. Xin, J. Correia, M. Veljkovic, Three-dimensional fatigue crack propagation simulation using extended finite element methods for steel grades S355 and S690 considering mean stress effects, *Eng. Struct.* 227 (2021) 111414. https://doi.org/10.1016/j.engstruct.2020.111414.
[43] International Organization for Standardization, Metallic materials-Fatigue testing-Fatigue crack growth method, 2018.
[44] D. Socie, G. Marquis, Multiaxial Fatigue, Society of Automotive Engineers, 2000.
[45] K. Yuki, T. Tadahisa, T. Seiichiro, B. Ayang, Experimental study for the effect of additional weld on fatigue strength in out-of-plane gusset welded joints, 38 (2) (2020) 139-143. https://doi.org/10.2207/qjjws.38.139s.
[46] B. Qiang, Y. Li, C. Yao, X. Wang, Through-thickness welding residual stress and its effect on stress intensity factors for semi-elliptical surface cracks in a butt-welded steel plate, *Eng. Fract. Mech.* 183 (2018) 106738. https://doi.org/10.1016/j.engfracmech.2018.02.016.
[47] J. Becker, K. Berg, M. Røder, K. Brasso, P. Iversen, A new finite element model for welding heat sources, *Scand. J. Urol.* 52 (1) (2018) 1-7. https://doi.org/10.1080/21681805.2017.1363816.
[48] J. Shen, Z. Chen, Welding simulation of fillet-welded joint using shell elements with section integration, *J. Mater. Process. Technol.* 214 (11) (2014) 2529-2536. https://doi.org/10.1016/j.jmatprotec.2014.04.034.
[49] T. Mori, H. Shimanuki, M. Tanaka, Influence of steel static strength on fatigue strength of web-gusset welded joints with UIT, *J. Japan Soc. Civ. Eng.* 3 (2015) 115-127. https://doi.org/10.2208/journalofjsce.3.1_115.
[50] I. Kim, H. Kim, D. Dao, J. Ahn, Y. Jeong, Fatigue resistance improvement of welded joints by bristle roll-brush grinding, *Int. J. Steel Struct.* 18 (5) (2018) 1631-1638. https://doi.org/10.1007/s13296-018-0059-1.
[51] I. Kim, Fatigue strength improvement of longitudinal fillet welded out-of-plane gusset joints using air blast cleaning treatment, *Int. J. Fatigue* 48 (2013) 289-299. https://doi.org/10.1016/j.ijfatigue.2012.11.010.
[52] N. Ma, K. Nakacho, T. Ohta, N. Ogawa, A. Maekawa, H. Huang, H. Murakawa, Inherent strain method for residual stress measurement and welding distortion prediction, *Proceedings of the ASME 2016 35th International Conference on Ocean, Offshore and Arctic Engineering*, 2016. https://doi.org/10.1115/omae2016-54184.
[53] S. Tanaka, T. Kawahara, H. Okada, Study on crack propagation simulation of surface crack in welded joint structure, *Mar. Struct.* 39 (2014) 315-334. https://doi.org/10.1016/j.marstruc.2014.08.001.
[54] R. Masoudi Nejad, M. Shariati, K. Farhangdoost, Prediction of fatigue crack propagation and fractography of rail steel, *Theor. Appl. Fract. Mech.* 101 (2019) 320-331. https://doi.org/10.1016/j.tafmec.2019.03.016.
[55] C. Cui, Q. Zhang, Y. Bao, Y. Bu, Y. Luo, Fatigue life evaluation of welded joints in steel bridge considering residual stress, *J. Constr. Steel Res.* 153 (2019) 509-518. https://doi.org/10.1016/j.jcsr.2018.11.003.
[56] Ž. Božić, S. Schmauder, H. Wolf, The effect of residual stresses on fatigue crack propagation in welded stiffened panels, *Eng. Fail. Anal.* 84 (2018) 346-357. https://doi.org/10.1016/j.engfailanal.2017.09.001.